frontiers | Frontiers in Chemistry

TYPE Original Research
PUBLISHED 03 October 2022
DOI 10.3389/fchem.2022.996116

OPEN ACCESS

EDITED BY
Yizhou Dong,
The Ohio State University, United States

REVIEWED BY
Hongyu Lin,
Xiamen University, China
Xinhui Su,
Zhejiang University, China

*CORRESPONDENCE
Jiqing Xuan,
xuanjiqing2021@163.com
Meng Ao,
aomeng735@163.com

†These authors have contributed equally to this work

SPECIALTY SECTION
This article was submitted to Medicinal and Pharmaceutical Chemistry, a section of the journal Frontiers in Chemistry

RECEIVED 17 July 2022
ACCEPTED 08 September 2022
PUBLISHED 03 October 2022

CITATION
Tang X, Li X, Li M, Zhong X, Fu W, Ao M and Xuan J (2022), Enhanced US/CT/MR imaging of integrin $\alpha_v\beta_3$ for liver fibrosis staging in rat.
Front. Chem. 10:996116.
doi: 10.3389/fchem.2022.996116

Enhanced US/CT/MR imaging of integrin $\alpha_v\beta_3$ for liver fibrosis staging in rat

Xueyao Tang[1,2†], Xuan Li[1,3†], Mingxing Li[1], Xiaoling Zhong[4], Wenguang Fu[5,6], Meng Ao[7]* and Jiqing Xuan[1]*

[1]Department of Ultrasound, The Affiliated Hospital of Southwest Medical University, Luzhou, China, [2]Department of Ultrasound, The Third People's Hospital of Chengdu, Clinical College of Southwest Jiao Tong University, The Second Affiliated Chengdu Hospital of Chongqing Medical University, Chengdu, China, [3]Department of Ultrasound, Sichuan Provincial People's Hospital, Chengdu, China, [4]Department of Gastroenterology, The Affiliated Hospital of Southwest Medical University, Luzhou, China, [5]Academician (Expert) Workstation of Sichuan Province, The Affiliated Hospital of Southwest Medical University, Luzhou, China, [6]Department of Hepatobiliary Surgery, The Affiliated Hospital of Southwest Medical University, Luzhou, China, [7]Department of Ultrasound, The Second Affiliated Hospital of Chongqing Medical University & Chongqing Key Laboratory of Ultrasound Molecular Imaging, Chongqing, China

Liver fibrosis is a global health challenge with high morbidity and mortality rates, and diagnostic sensitivity of liver fibrosis tests can be increased using multimodal molecular agents. We designed cyclic arginine-glycine-aspartic acid (cRGD)-modified nanoparticles (NPs) using ultrasound (US)/computed tomography (CT)/magnetic resonance (MR) triple-modality imaging to evaluate liver fibrosis stages. *In vitro* and *in vivo* studies were conducted using primary hepatic stellate cells (HSCs) and a rat model of liver fibrosis induced by carbon tetrachloride (CCl_4). Our results showed cRGD-poly(lactic-co-glycolic acid)-Fe_3O_4-perfluorocarbon bromide (cRGD-PLGA-Fe_3O_4-PFOB) NPs were preferentially internalised by activated HSCs (aHSCs). The main cell types expressing integrin $\alpha_v\beta_3$ during liver fibrogenesis were the aHSCs. The protein levels of α_v and β_3 expressed on aHSCs increased with the progression of liver fibrosis. After intravenous injection of cRGD-PLGA-Fe_3O_4-PFOB NPs, the echo intensity (EI) values, CT values, and T2 values of liver parenchyma correlated well with liver fibrosis severity. cRGD-PLGA-Fe_3O_4-PFOB NPs as multifunction contrast agents showed great potential to reflect the degree of HSC activation and distinguish among different liver fibrotic stages. The ligand-directed and integrin $\alpha_v\beta_3$-mediated accumulation provides active and passive targeting capabilities, permitting the targeted multimodal imaging of cRGD-PLGA-Fe_3O_4-PFOB NPs, which delivers accurate non-invasive diagnosis and real-time monitoring of liver fibrosis development.

KEYWORDS

integrin $\alpha_v\beta_3$, hepatic stellate cell, liver fibrosis, nanoparticles contrast agent, multi-mode molecular imaging

1 Introduction

Liver fibrosis, a typical complication of various chronic injuries characterised by excessive synthesis and deposition of extracellular matrix (ECM) proteins, is one of the main causes of mortality and morbidity, affecting over 1,300 million people across the world (Friedman, 2008; Yoon, et al., 2016; Wang, et al., 2014; Williams, 2006). If the underlying aetiologies are eliminated early enough, followed by subsequent aggressive treatments, liver fibrosis may be reversed, otherwise, it will progress to cirrhosis and even liver cancer (Lin, 2017). Such conditions emphasise the urgent need for early detection of liver fibrosis. To date, liver biopsy is the most reliable approach for assessing the severity of liver fibrosis. However, this technique samples a limited liver volume and can only be performed at limited frequencies, out of concern for the incidence of complications (Patel and Rockey, 2006). Clinical biomedical imaging techniques have the potential to enable minimally invasive assessments of liver fibrosis (Cassinotto, et al., 2016; Shin, et al., 2018; Tapper and Loomba, 2018). Clinical techniques hold great promise for anatomical or structural imaging include, but are not limited to, US, CT and MR imaging, whereas their sensitivities are insufficient to detect early liver fibrosis because of their high reliance on hepatic morphological changes (Li et al., 2015; Zhang et al., 2016). Molecular imaging (or functional imaging), which involves the *in vivo* detection of molecular processes, enzymes, and receptors, can detect liver fibrosis at the cellular or molecular level and increase diagnostic sensitivity (Taymouri and Taheri, 2016; Petros and DeSimone, 2010).

Activation of HSCs is a key step in the development of liver fibrosis. In response to various chronic injury factors, the vitronectin receptor integrin $\alpha_v\beta_3$ drives fibrogenic activation of HSCs (Taymouri and Taheri, 2016). It has been well recognized that the integrin $\alpha_v\beta_3$ can interact with ECM components via the RGD tri-peptide sequence and the up-regulation of integrin $\alpha_v\beta_3$ is intimately related to the extent of fibrosis. Consequently, as previous studies demonstrated, a cRGD-based integrin $\alpha_v\beta_3$ specific molecular probe can be an effective tool for noninvasive assessment of fibrosis progression or therapeutic response (Li, et al., 2011; Zhang, et al., 2017; Xuan, et al., 2017; Li, et al., 2016). Nonetheless, to the best of our knowledge, the majority of such agents only loaded with one imaging material and implemented in a single imaging technique.

PFOB, a liquid perfluorocarbon with a higher density than water, is a viable candidate to be used for multimodal imaging. Owing to their low acoustic velocity and high density, aggregated PFOB microspheres can substantially enhance acoustic reflection (Andre, et al., 1990; Tran, et al., 2007). Moreover, the presence of bromine in the PFOB carbon linear chain allows its detection using CT (Mattrey et al., 1982). Superparamagnetic iron oxide NPs mainly contain iron oxides, Fe_3O_4 and Fe_2O_3, which have good magnetic sensitivity, and can reduce the transverse relaxation time (Mattrey et al., 1982). In order to improve the independent imaging mode, herein we adopted cRGD-modified PLGA carrying PFOB and Fe_3O_4 in our study to get a multimodal US, MR, and CT contrast agent. In present study, we isolated primary rats HSCs to explore the ability of cRGD-PLGA-Fe_3O_4-PFOB NPs to target integrin $\alpha_v\beta_3$ on aHSCs. Further, we compared US/CT/MR molecular imaging results with histological analysis and liver integrin $\alpha_v\beta_3$ levels to evaluate the feasibility of targeted multimodal molecular imaging as a non-invasive method for early diagnosis and staging liver fibrosis in CCl_4 rat models.

2 Materials and methods

2.1 Preparation of cRGD-PLGA-Fe_3O_4-PFOB NPs

PLGA-Fe_3O_4-PFOB NPs were fabricated using a double emulsion evaporation process. Briefly, 60 μL Fe_3O_4, 30 μL PFOB and 50 mg PLGA-PEG-COOH (LA/GA = 50:50, MW = 12,000, Daigang, China) were codissolved in 1 ml of methylene chloride. The solution was emulsified for 4 min using probe sonication (SONICS and MATERALS Inc., Newtown, CT, United States) under 13% output amplitude setting (5 s on and 5 s off). Then, the solution was poured into 5 ml cold poly (vinyl alcohol) (MW = 25,000; Sigma, St. Louis, MO, United States) solution (5% w/v), followed by a secondary emulsification under the same conditions. After adding 10 ml isopropanol solution (2% w/v), the emulsion was magnetically stirred for 6 h (300 rpm, 20–25°C) to extract dichloromethane and isopropanol. PLGA-Fe_3O_4-PFOB NPs were obtained after centrifugation at 10,000 rpm and washed three times with deionised water. The steps of cRGD conjugating to PLGA-Fe_3O_4-PFOB NPs were the same as our previous study (Xuan, et al., 2017). For confocal microscopy, 50 μL concentrated Nile red solution (0.057 mg/ml in methylene chloride) was added to the organic solution prior to emulsification. The morphological and structural characteristics of NPs were imaged using optical microscopy (CKX41, Olympus, Tokyo, Japan), transmission electron microscopy (TEM, H-7600, Japan), and scanning electron microscopy (SEM, JEM-7800F, Tokyo, Japan). The mean size and zeta potential measurements were performed using a laser particle size analyser system (Zeta SIZER 3000HS: Malvern, United Kingdom). The amount of Fe in the NPs was quantified using atomic absorption spectroscopy.

2.2 Detection of conjugation efficiency of cRGD and PLGA-Fe_3O_4-PFOB NPs

The Nile Red-labelled PLGA and FITC-labelled cRGD were used for confocal microscopy (CLSM, AIR, Japan) observations.

The diluted cRGD-PLGA-Fe_3O_4-PFOB NPs were dropped onto a Petri dish and observed under excitation at 543 and 488 nm, respectively. The binding rate of the FITC-labelled cRGD peptide towards PLGA-Fe_3O_4-PFOB was further quantitatively evaluated via flow cytometry (FCM, FACS-Calibur, United States) with blank PLGA-Fe_3O_4-PFOB NPs as control, and the excitation was set at 488 nm.

2.3 *In vitro* cytotoxicity of cRGD-PLGA–Fe_3O_4–PFOB NPs

Cell viability was detected using a cell counting kit-8 (CCK-8) cell viability assay (Dongren Chemical & Tech Co., Ltd., China). BRL-3A cells (Procell Life Sci & Tech Co., Ltd., China) were first seeded in a 96-well culture plate at a density of 5×10^3/well and incubated for 24 h. Then, the medium was switched to a mixed medium containing varying concentrations of cRGD-PLGA-Fe_3O_4-PFOB NPs (20, 10, 5, 2.5, 1.25, 0.625, and 0.3125 g/L). Wells without cells or NPs served as blank controls. After 24h, the CCK-8 was added (100 μL) to each well and incubated for 4 h. Finally, the absorbance (A) of each well was measured using a microplate reader (Molecular Devices, United States) at 570 nm.

2.4 *In vitro* US/CT/MR imaging

In vivo US imaging was performed using a commercial US imaging system (Vevo LAZR, Visual Sonics Inc., Canada). PLGA-Fe_3O_4-PFOB NPs aqueous solutions at varying concentrations (50, 25, 12.5, 6.25, and 0 mg/ml) were injected into Eppendorf tubes (EPs, 2 ml). The images were obtained under the same parameter settings (imaging depth = 3.5 cm, mechanical index = 0.1, frequency range: 13–21 MHz). A DFY-type ultrasonic image quantitative analyser (Institution of Ultrasound Imaging of Chongqing Medical University, China) was used to quantify the EI values for each sample. *In vitro* CT imaging was performed using a CT scanner (LightSpeed VCT, GE, United States). EPs filled with diluted suspension were placed in a skull coil and scanned at the same parameter settings: tube current = 180 mA, tube voltage = 110 kV, layer thickness = 0.625 mm. The concentrations of PLGA-Fe_3O_4-PFOB NPs suspensions were 50, 25, 12.5, 6.25, and 0 mg/ml, respectively. GE ADW4.4 software was used to measure and compare the CT values of different samples. MR imaging was performed using a clinic 3.0 T MR scanner (Philips, United States). Samples with different iron concentrations (1750, 1,500, 1,250, 1,000, 750, 500, 250, and 0 mg/L) were prepared. Imaging parameters were as follows: repetition time (TR) = 250 ms, echo time (TE) = 15 ms, matrix = 256 mm × 192 mm, slice thickness = 4 mm. The T2 signal intensity values were measured and compared.

2.5 Cell-targeting ability of cRGD-PLGA-Fe_3O_4-PFOB *in vitro*

HSCs were isolated from rats by collagenase digestion followed by OptiPrep density gradient centrifugation (Sun, et al., 2006; Jeong, et al., 2006; Horiguchi, et al., 2008). After 48 h, primary quiescent HSCs (qHSCs) showed features of myofibroblasts and were therefore identified as aHSCs. Primary rat HSCs cultured for 24 and 48 h were applied for further experiments. After incubation for 30 min with cRGD-PLGA-Fe_3O_4-PFOB NPs (25 mg/ml), cells were washed with phosphate-buffered saline (PBS), fixed in 4% paraformaldehyde, and incubated overnight with primary rabbit glial fibrillary acidic protein (GFAP, diluted 1:200, Abcam, United Kingdom) and primary rabbit *α*-smooth muscle actin (α-SMA, diluted 1:200, Abcam, United Kingdom) at 4°C. The secondary antibody selected for visualisation was FITC-conjugated goat anti-rabbit antibody (1: 200; Abcam, United Kingdom). 4′6-diamindino-2-phenylindole (DAPI) was used to dye the cell nuclei. Finally, the ability of cRGD-PLGA-Fe_3O_4-PFOB NPs to target HSCs was observed via CLSM.

2.6 Animal models

To establish the liver fibrosis model, eight-week-old female Sprague Dawley rats (200 ± 20 g, Chengdu Dashuo Experimental Animal Co., Ltd., China) were subcutaneously injected with CCl_4 solution in the back (40% in olive oil, the first dosage: 5 ml/kg, the others: 3 ml/kg) twice weekly for either 3, 6, or 9 weeks (n = 12 per group). Controls received normal saline. All experiments were conducted following the guidelines for the care and use of laboratory animals approved by the Ethical Committee of Southwest Medical University.

2.7 Biosafety of cRGD-PLGA-Fe_3O_4-PFOB NPs

Six normal rats received 50 mg/ml cRGD-PLGA-Fe_3O_4-PFOB NPs at a dose of 5 ml/kg, administered by means of tail vein injection. Serum was collected before and 1 day after injection. Detected biochemical indicators included alanine aminotransferase (ALT), aspartate aminotransferase (AST), total protein (TP), blood urea nitrogen (BUN), creatinine (SCr), andglomerular filtration rate (GFR).

2.8 *In vivo* US/CT/MR imaging

Rats with the same administration time were randomly divided into two subgroups. Rats in one group were

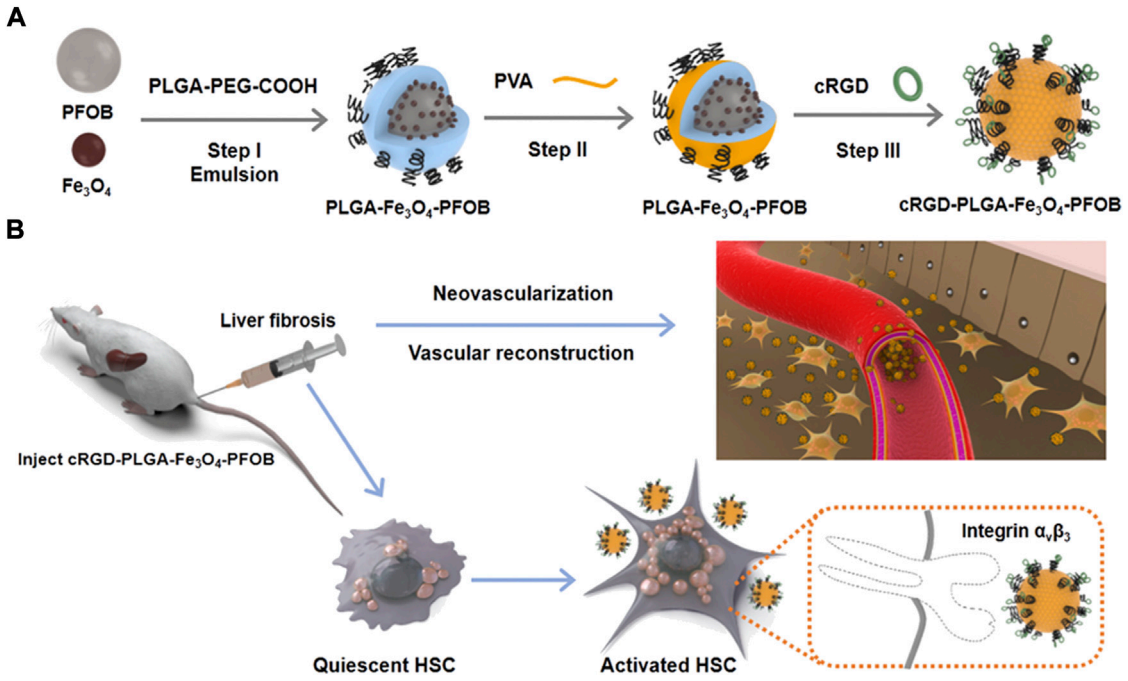

FIGURE 1
Schematic illustration of fabrication process of **(A)** cRGD-PLGA-Fe_3O_4-PFOB NPs and **(B)** their targeting capabilities to integrin $\alpha_v\beta_3$ expressed by aHSCs.

administered cRGD-PLGA-Fe_3O_4-PFOB NPs while another group received PLGA-Fe_3O_4-PFOB NPs. The dose of NPs was set at 5 ml/kg body weight. We first determined an appropriate observed time point by comparing the liver quantitative index of US/CT/MR within 48 h after PLGA-Fe_3O_4-PFOB NPs injection. All rats were anaesthetised by intraperitoneal injection of 3% pentobarbital sodium at 1 ml/kg. Given the small volume of the rat liver, the right liver parenchyma at the maximum cross-section of the liver was selected as the region of interest (ROI) for quantitative analysis.

In vivo US was performed using an ultrasonic diagnostic instrument (Esaote MyLab90, Florence, Italy) in routine B mode. The concentration of NPs was 50 mg/ml. Imaging parameters were as follows: frequency = 10 MHz, mechanical index = 0.1, depth = 44 mm, total gain = 86%. An ultrasonic quantitative analysis diagnostic system (Chongqing Medical University, Chongqing, China) was used to quantitatively measure the EI in the ROI in the liver parenchyma. For CT imaging, the imaging parameters were as follows: tube voltage = 100 kV, tube current = 170 mA, section thickness = 5 mm. The concentration of NPs was 50 mg/mL. GE ADW 4.3 software was used to measure the CT values in the ROI. When rats were subjected to MR imaging, the contrast concentration was adjusted to 10 mg/ml based on the image effect. Liver images were obtained before and after injection using the T2WIM-GRASE sequence. The following parameters were used: TR = 1,100 ms, TE = 20 ms, matrix = 180 × 180; slice thickness = 2 mm; field of view = 120 mm × 120 mm. The T2 values from the T2 map images automatically reconstructed by the system were measured and compared.

2.9 Histological analysis of hepatic fibrosis

The livers tissues were fixed in neutralised formalin and embedded in paraffin. The liver sections were stained with haematoxylin and eosin (HE) and Masson's trichrome and then observed by light microscope (Olympus DP27, Japan). Further semi-quantitative analysis was carried out using image analysis software (Image-Pro Plus 6.0, Media Cybernetics Inc., Silver spring, MD, United States), which could measure the areas of Masson's trichrome staining (fibrotic).

2.10 Immunofluorescence staining

The slices were permeated with 0.5% Triton X-100. Primary antibodies against rat $\alpha_v\beta_3$ integrin (diluted 1:50, Abcam, United Kingdom), anti-mouse α-SMA antibody (diluted 1:400, Abcam, United Kingdom), and anti-mouse CD31 antibody (diluted 1:50, Abcam, United Kingdom) were used. Secondary antibodies included Alexa Fluor 647-conjugated goat anti-rabbit (diluted 1:400, Abcam, United Kingdom) and FITC-conjugated

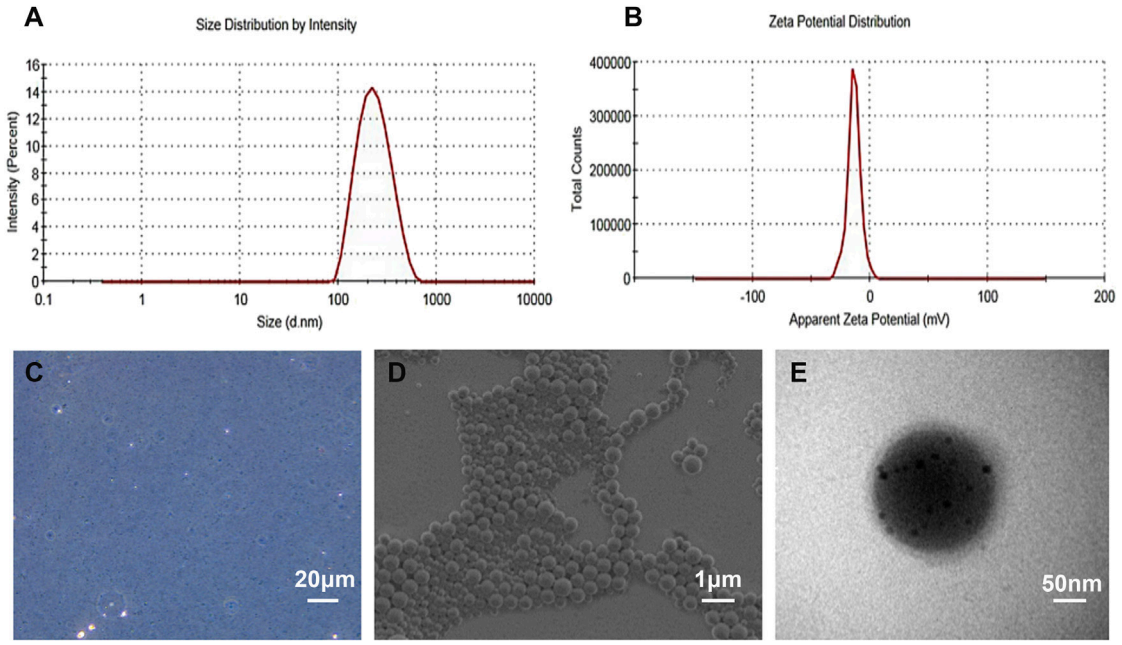

FIGURE 2
Characterization of the as-prepared NPs. **(A)** DLS size distribution of cRGD-PLGA-Fe_3O_4-PFOB NPs. **(B)** The zeta potential of cRGD-PLGA-Fe_3O_4-PFOB NPs. **(C)** Light microscopy image of cRGD-PLGA-Fe_3O_4-PFOB NPs. **(D)** SEM image of cRGD-PLGA-Fe_3O_4-PFOB NPs. **(E)** TEM image of cRGD-PLGA-Fe_3O_4-PFOB NPs.

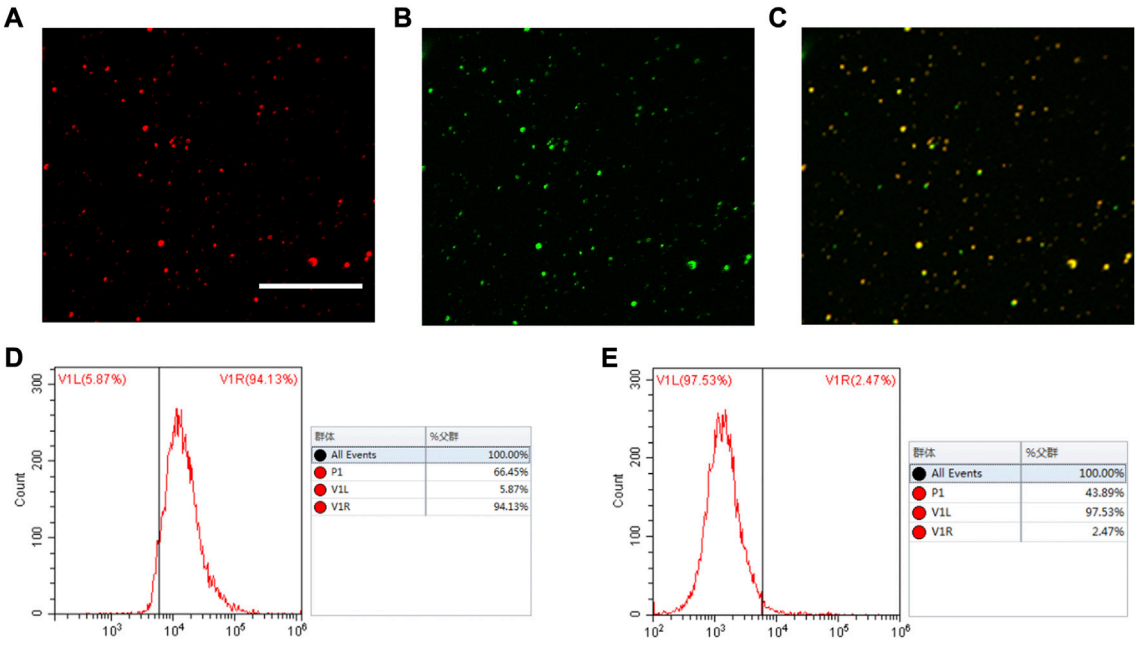

FIGURE 3
CLSM and FCM images of the cRGD-PLGA-Fe_3O_4-PFOB NPs. **(A)** Nile red (×400; Scale: 50 μm). **(B)** FITC. **(C)** Merge. **(D)** FCM image of PLGA-Fe_3O_4-PFOB NPs modified with FITC-labelled cRGD peptide. **(E)** FCM image of PLGA-Fe_3O_4-PFOB NPs.

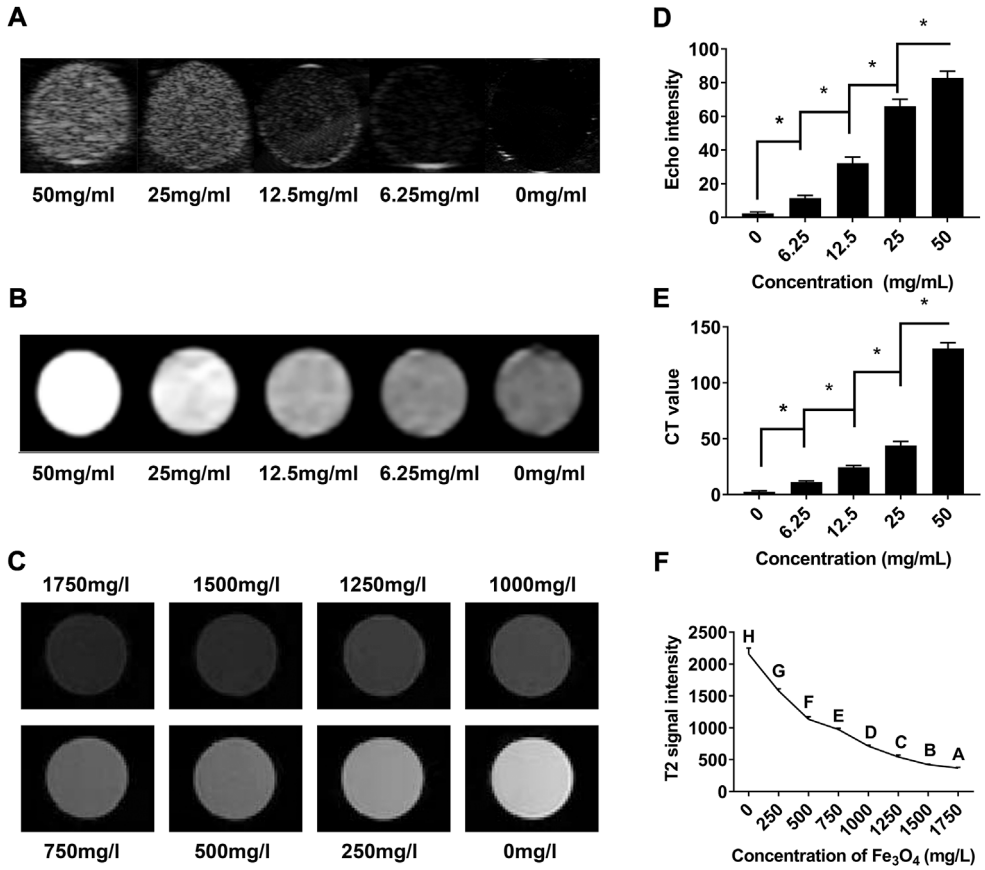

FIGURE 4
In vitro assessment of cRGD-PLGA-Fe_3O_4-PFOB NPs. **(A)** US images of cRGD-PLGA-Fe_3O_4-PFOB NPs at different concentrations. **(B)** CT images of cRGD-PLGA-Fe_3O_4-PFOB NPs at different concentrations. **(C)** T2-weighted MR images of cRGD-PLGA-Fe_3O_4-PFOB NPs at different Fe concentrations in water. **(D)** Echo intensity of cRGD-PLGA-Fe_3O_4-PFOB NPs at different concentrations. **(E)** CT values of cRGD-PLGA-Fe_3O_4-PFOB NPs at different concentrations. **(F)** T2 signal intensity of cRGD-PLGA-Fe_3O_4-PFOB NPs at different Fe concentrations in water.

mouse anti-rat secondary antibodies (diluted 1:400, Abcam, United Kingdom). The liver sections were incubated with mixed primary antibody, mixed secondary antibody, and DAPI. After washing with PBS, the slides were mounted using an anti-fluorescence quencher. Multicoloured fluorescent staining images were analysed via CLSM. The mean fluorescence densities of liver sections were calculated using Image-Pro Plus 6.0. For each group, three amplifying fields (400) were randomly chosen to conduct a semi-quantitative analysis of integrin $\alpha_v\beta_3$, α-SMA, and CD31 expression levels.

2.11 Western blotting

The frozen specimens were lysed in radioimmunoprecipitation assay buffer on ice. After centrifugation, the protein concentration in the supernatant was determined with a bicinchoninic acid protein assay kit. Forty micrograms of total protein were subjected to SDS-PAGE (sodium dodecyl sulfate-polyacrylamide gel electrophoresis) on 10% gels and transferred to a polyvinylidene fluoride membrane. A 5% skimmed milk blocking solution was used to block the cell membrane. Proteins were probed with primary antibodies (α-SMA = 1: 500, αv = 1: 5,000, β3 = 1: 1,000, β-actin = 1: 100,000) overnight at 4°C, followed by horseradish peroxidase-conjugated secondary antibodies. Immunoreactive band quantification was conducted using an enhanced chemiluminescence assay. Glyceraldehyde-3-phosphate dehydrogenase (GAPDH) was used as an internal reference, and the amounts of integrin α_v, integrin β_3, and α-SMA protein were determined and expressed as a ratio relative to the GAPDH content.

2.12 Statistical analysis

All quantitative data are presented as mean ± standard deviation (SD). Differences were tested using one-way analysis of variance (ANOVA) or Student's *t*-tests in SPSS statistical

TABLE 1 Serum biochemical indicators post cRGD-PLGA-Fe_3O_4-PFOB NPs injection (50 mg/ml).

Indicators	Pre-injection	Post-injection
ALT (U/L)	46.53 ± 12.08	52.75 ± 14.39
AST (U/L)	122.48 ± 36.02	155.50 ± 40.55
TP (g/L)	52.02 ± 4.99	53.45 ± 4.34
GFR (ml/min)	218.40 ± 9.54	215.72 ± 12.10
SCr (μmol/L)	28.33 ± 2.89	29.32 ± 3.68
BUN (mmol/L)	5.33 ± 0.99	5.13 ± 0.30

Note: pairwise comparisons of the same indicators before and after injection (all $p > 0.05$).

package (Version 13.0, SPSS Inc. Chicago, IL, United States). Statistical significance was set at $p < 0.05$.

3 Results and Discussion

3.1 Characterisation of cRGD-PLGA-Fe_3O_4-PFOB NPs

cRGD-PLGA-Fe_3O_4-PFOB NPs was prepared as previously reported by Xuan and Dong (Xuan, et al., 2017; Dong, et al., 2019), with slight modifications. Figure 1A shows the schematics of the cRGD-PLGA-Fe_3O_4-PFOB NPs. Figure 1B shows the targeting process of the cRGD-PLGA-Fe_3O_4-PFOB NPs to integrin $\alpha_v\beta_3$ *in vivo*. We chose PLGA-PEG-COOH as the carrier. The addition of PEG reduced the recognition by the reticuloendothelial system and the immune system, which prolonged the blood circulation time *in vivo*. On average, all NP preparations were approximately 221 nm in size, and the polydispersity index was below 0.20, verifying size homogeneity (Figure 2A). The zeta potential was −9.3 ± 4.3 mV (Figure 2B). The optical microscope image (Figure 2C) showed that the NPs were small spheres and distributed evenly in the suspension, indicating that they attained uniform size and good dispersion. Dynamic light scattering (DLS) size and optical morphology were verified via SEM (Figure 2D), which revealed a uniform spherical morphology with smooth surfaces. To investigate whether PFOB and Fe_3O_4 could be successfully loaded into PLGA, diluted NP suspension samples were observed via TEM. As shown in Figure 2E, the prepared NPs appeared as a core-shell structure with several black iron particles distributed on the shell membrane. Meanwhile, a significant density difference between the shell and the core indicated that PFOB was effectively encapsulated in PLGA NPs. Furthermore, the loading rate of Fe_3O_4 was calculated as approximately 38%, according to the atomic absorption spectrometry results.

3.2 Conjugation efficiency of cRGD on PLGA-Fe_3O_4-PFOB NPs

The technique used to conjugate cRGD peptides to the PLGA-Fe_3O_4-PFOB NP surface was derived from the carbodiimide method described in previous reports (Xuan,

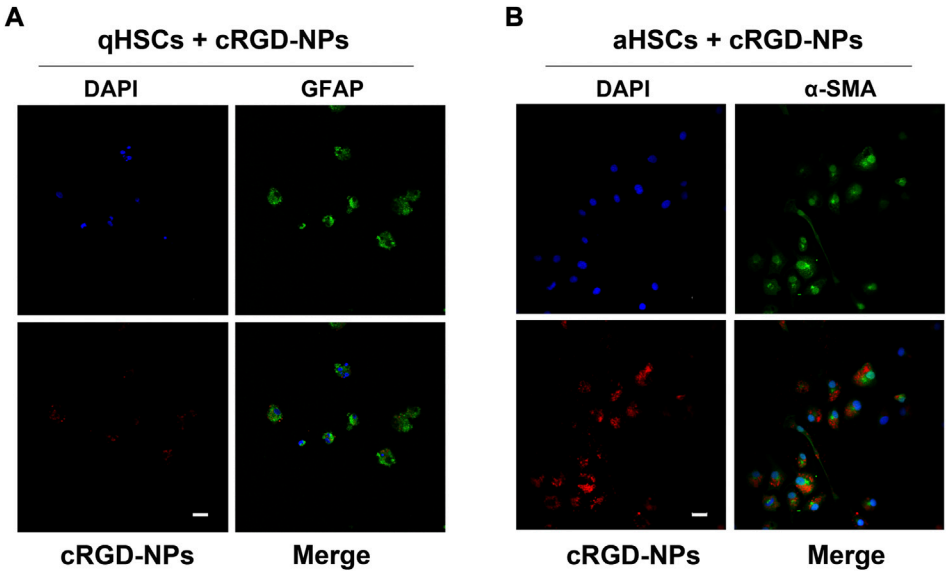

FIGURE 5
Representative fluorescent images of qHSCs **(A)** and aHSCs **(B)** incubated with 25 mg/ml of cRGD-PLGA-Fe_3O_4-PFOB NPs (red) solution for 30 min at 37°C in the dark (×400; Scale: 100 μm).

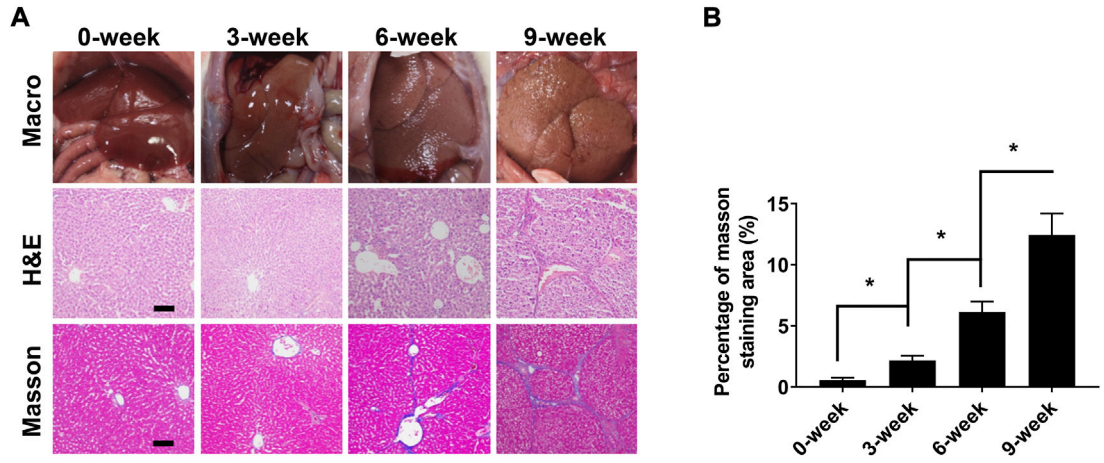

FIGURE 6
Liver fibrosis stage analysis after 0, 3, 6, and 9 weeks of CCl_4 induction. **(A)** Macroscopic inspections and pathological examination of the liver fibrosis and control groups (×100; Scale: 100 μm). **(B)** Semi quantitative analysis of Masson's trichrome staining (fibrosis) in normal and fibrotic livers. *$p < 0.05$.

et al., 2017; Sanna, et al., 2013). This covalent binding mode was stable, effective, and not greatly influenced by the shear flow in blood circulation. To visualise whether cRGD could be successfully connected to PLGA, Nile Red-tagged PLGA-Fe_3O_4-PFOB NPs and FITC-labelled cRGD were used. The CLSM image shows that the localisation of PLGA-Fe_3O_4-PFOB NPs (red) largely overlapped with cRGD (green), and the overlapping areas were bright yellow in colour (Figures 3A–C). Next, we performed FCM analysis to further verify the CLSM results. As illustrated in Figure 3D, the FITC positive rate of cRGD-PLGA-Fe_3O_4-PFOB NPs was 94.13%. Compared to the NPs without cRGD (only 2.47%, Figure 3E), the FITC positive rate was also significantly higher. Both the CLSM and FCM findings indicated that the cRGD was successfully conjugated onto PLGA-Fe_3O_4-PFOB NPs with an excellent connection rate.

3.3 *In vitro* US/CT/MR imaging

To investigate the US/CT/MR imaging capacities of cRGD-PLGA-Fe_3O_4-PFOB NPs *in vitro*, we first observed the images of EPs containing suspension with different concentrations in an agarose gel model. EPs filled with higher concentrations of NPs suspensions appeared brighter in US and CT images and dimmer in MR images (Figures 4A–C). Quantitative analysis results showed that the EI and CT values increased with increasing NP concentrations, whereas the T2 signal intensity values decreased (Figures 4D–F). These findings confirmed that the cRGD-PLGA-Fe_3O_4-PFOB NPs contain the imaging properties of PFOB and Fe_3O_4 and have the potential to serve as US/CT/MR multimodality contrast agents for *in vivo* applications.

3.4 Cytotoxicity and acute biosafety of cRGD-PLGA-Fe_3O_4-PFOB NPs

To verify the cytotoxicity of cRGD-PLGA-Fe_3O_4-PFOB NPs, BRL-3A cells were incubated in cell-culture media, which contain cRGD-PLGA-Fe_3O_4-PFOB NPs. All the treated cells exhibited similar morphologies. The BRL-3A cell viability was measured as (88.69 ± 2.71)% (88.68 ± 4.17)%, (100.01 ± 7.65)% (89.93 ± 5.16)%, (98.23 ± 6.77)% (92.29 ± 4.95)%, and (96.18 ± 8.23)% for groups cultured with cRGD-PLGA-Fe_3O_4-PFOB NPs at concentrations of 20, 10, 5, 2.5, 1.25, 0.625, and 0.3125 mg/ml, respectively. These results did not show a specific correlation between NP concentrations and cell viability, nor did they display a significant difference among NP groups in contrast to the control group ($p > 0.05$), implying that NPs were almost non-toxic over each concentration range. To further verify the acute biosafety of cRGD-PLGA-Fe_3O_4-PFOB NPs *in vivo*, the tail veins of the rats were injected with a dosage of 5 mL/kg from 50 mg/ml NPs suspensions. No significant changes were observed in the serum biochemical indicators (liver and kidney function) 24 h post-injection (Table 1). These results were in good agreement with the cytotoxicity assays, indicating that intravenously injected cRGD-PLGA-Fe_3O_4-PFOB NPs are biocompatible.

3.5 Binding characterization of cRGD-PLGA-Fe_3O_4-PFOB NPs *in vitro*

cRGD peptides are known as one of the most effective functioning elements for delivering diagnostic 'probes' into fibrotic livers owing to their rich receptor capacity and

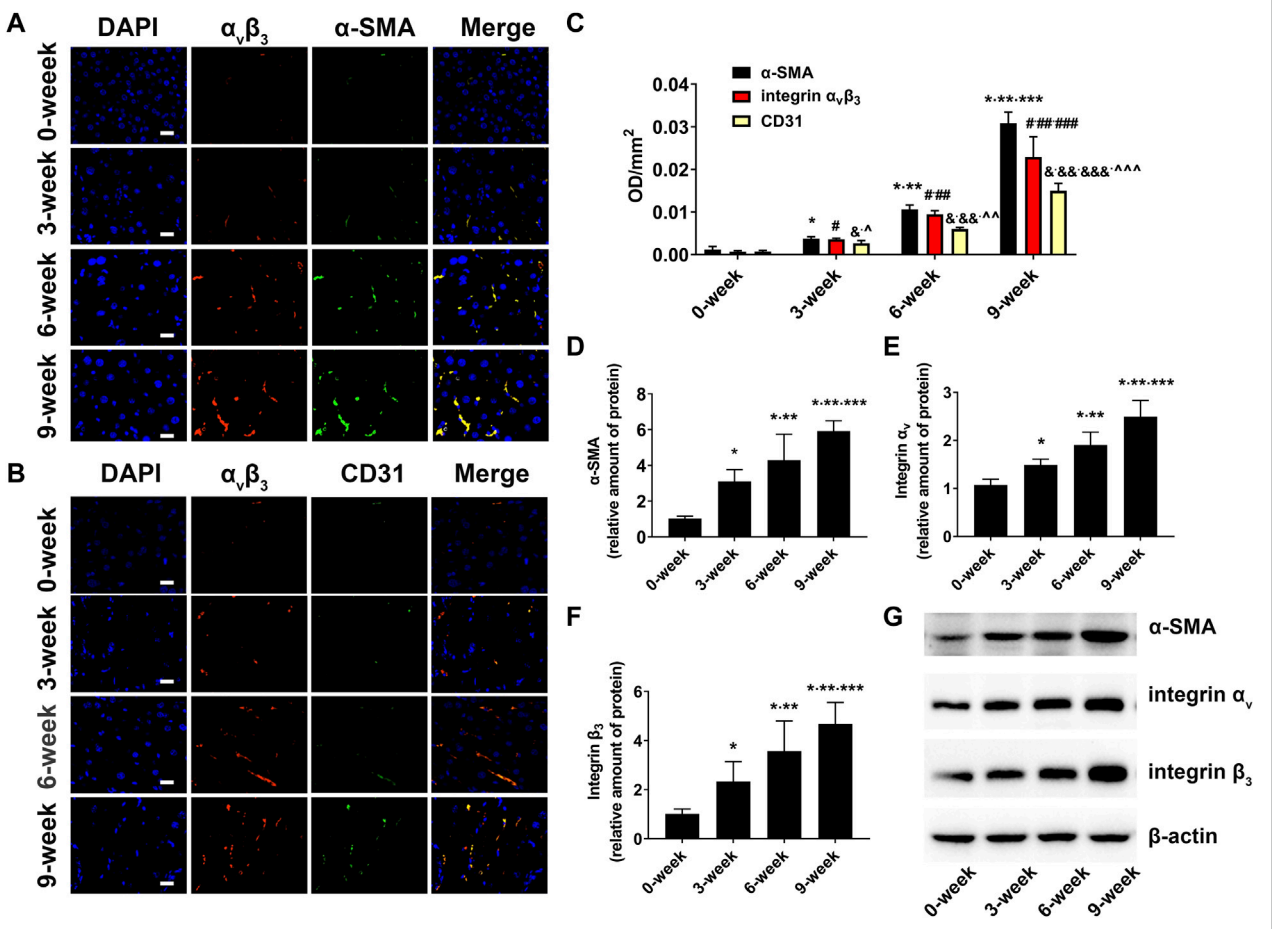

FIGURE 7
Biomarker expression in fibrotic livers **(A)** Immunofluorescent colocalisation of integrin $\alpha_v\beta_3$ and α-SMA in the liver fibrosis groups and control group (×400; Scale: 20 μm). **(B)** Immunofluorescent colocalisation of integrin $\alpha_v\beta_3$ and CD31 in the liver fibrosis groups and control group (×400; Scale: 20 μm). **(C)** Comparison of mean fluorescence densities of integrin $\alpha_v\beta_3$, α-SMA and CD31 in the liver fibrosis groups and control group (*p < 0.05 versus 0-week group; **p < 0.05 versus 3-week group; ***p < 0.05 versus 6-week group; #p < 0.05 versus 0-week group; ##p < 0.05 versus 3-week group; ###p < 0.05 versus 6-week group; &p < 0.05 versus 0-week group; &&p < 0.05 versus 3-week group; &&&p < 0.05 versus 6-week group; ^p < 0.05 versus α-SMA in the 3-week group; ^^p < 0.05 versus α-SMA in the 6-week group); ^^^p < 0.05 versus α-SMA in the 9-week group). **(D–G)** Comparison of the protein level of α-SMA, α_v and β_3 integrin subunits by western blot in the liver fibrosis groups and control groups (**p < 0.05 versus 0-week group; ***p < 0.05 versus 3-week group; ****p < 0.05 versus 6-week group).

prominent receptor-coupling affinity to integrin $\alpha_v\beta_3$ receptors (Li, et al., 2011; Zhang, et al., 2017; Xuan, et al., 2017). As reported previously (Li, et al., 2011; Zhou, et al., 2004), integrin $\alpha_v\beta_3$ was highly expressed on aHSC membranes but was found at a very low expression level in qHSCs. To confirm the ability of cRGD–PLGA–Fe_3O_4–PFOB NPs to target aHSCs *in vitro*, we isolated primary HSCs from normal rats. As presented in the CLSM results (Figures 5A,B), aHSCs demonstrated significantly higher uptake of cRGD–PLGA–Fe_3O_4–PFOB NPs compared to qHSCs. Very low uptake of cRGD–PLGA–Fe_3O_4–PFOB NPs in qHSCs may be the result of passive uptake or nonspecific endocytosis. We demonstrated that adding cRGD peptide to NPs causes them to specifically target aHSCs *in vitro*, laying a foundation for targeted imaging *in vivo*.

3.6 Liver fibrosis stage analysis

During the 9 weeks of CCl_4 administration, liver fibrosis and disease progression was confirmed by anatomical visualisation upon dissection, histologic staining and areas measurements of collagen deposition (Figures 6A,B). No noticeable fibrosis changes were observed in the livers of the 0-weeks group. With prolonged CCl_4 administration, the structure of normal liver lobules was damaged, pseudo-lobules appeared, and the fibres surrounding the pseudo-lobules increased and widened significantly. Furthermore, the collagen deposition area increased with the prolonged period of CCl_4 injection. These results suggested that our animal model could effectively present the pathological progression of liver fibrosis.

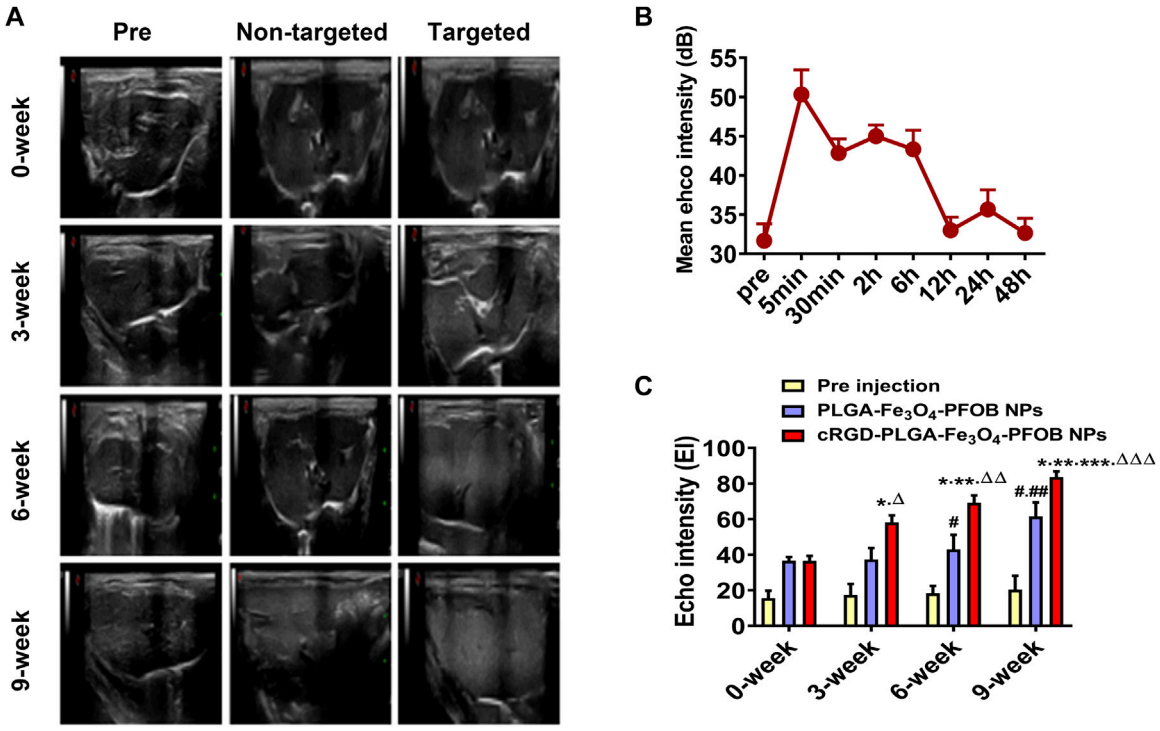

FIGURE 8
In vivo US imaging. **(A)** US images of liver before and after injection of targeted contrast agents (cRGD-PLGA-Fe_3O_4-PFOB NPs) or non-targeted contrast agents (PLGA-Fe_3O_4-PFOB NPs). **(B)** EI value of the liver parenchyma in the 0-week group within 48 h after injection of cRGD-PLGA-Fe_3O_4-PFOB NPs. **(C)** Comparison of liver EI values before and after injection of cRGD-PLGA-Fe_3O_4-PFOB NPs or PLGA-Fe_3O_4-PFOB NPs in each group (*$p < 0.05$ versus 0-week group, **$p < 0.05$ versus 3-week group, ***$p < 0.05$ versus 6-week group, #$p < 0.05$ versus 0-week or 3-week group, ##$p < 0.05$ versus 6-week group, ΔP <0.05 versus non-targeted 3-week group, ΔΔP <0.05 versus non-targeted 6-week group, ΔΔΔP <0.05 versus non-targeted 9-week group).

3.7 Biomarkers expression in fibrotic livers

To define the relationship between integrin $\alpha_v\beta_3$, α-SMA, CD31, and liver fibrosis, immunofluorescence staining and western blotting were conducted. The immunofluorescence staining images and the corresponding average optical density results are presented in Figures 7A–C. As expected, only weak fluorescence was observed in the control group, but the fluorescence intensity and area started to increase in the CCl_4-treated group from 3-week to 9-week, and the expression levels of $\alpha_v\beta_3$, α-SMA, and CD31 were consistent with the progression of liver fibrosis. The results of the western blotting were in line with those of the immunofluorescence staining (Figures 7D–G).

Since the expression of integrin $\alpha_v\beta_3$ is elevated upon both HSC activation and capillarisation of liver sinusoidal endothelial cells (LSECs) (Li, et al., 2011; Li, et al., 2016; Turaga, et al., 2021), overlay immunofluorescence staining of integrin $\alpha_v\beta_3$ and α-SMA, integrin $\alpha_v\beta_3$ and CD31 in fibrotic livers were performed to investigate the main factors of integrin $\alpha_v\beta_3$ up-regulation. α-SMA is recognised as a specific marker of aHSCs (Wu, et al., 2019). In addition, CD31, a characteristic symbol of LSECs, was rarely expressed in normal liver tissues but positively expressed in fibrotic livers owing to sinusoidal remodelling and intrahepatic angiogenesis (Li, et al., 2011; Li, et al., 2016; Connolly, et al., 2010). In our study, the overlapped areas of integrin $\alpha_v\beta_3$ and α-SMA were significantly larger than those of integrin $\alpha_v\beta_3$ and CD31. This result was further supported by a higher average optical density value of α-SMA compared to CD31 in the fibrosis groups. Therefore, we assumed that aHSCs may be primary cells expressing integrin $\alpha_v\beta_3$ during liver fibrosis, and the increased integrin $\alpha_v\beta_3$ was more closely related to the activation of HSCs than neovascularization.

3.8 *In vivo* US/CT/MR imaging and image analysis

To further verify the effect of the cRGD-PLGA-Fe_3O_4-PFOB NPs on liver fibrosis staging *in vivo*, US, CT, and MR imaging were performed on the CCl_4 rat models. All liver images before and 6 h after injection were captured and stored (Figures 8A, 9A, 10A). No significant differences in EI were observed among

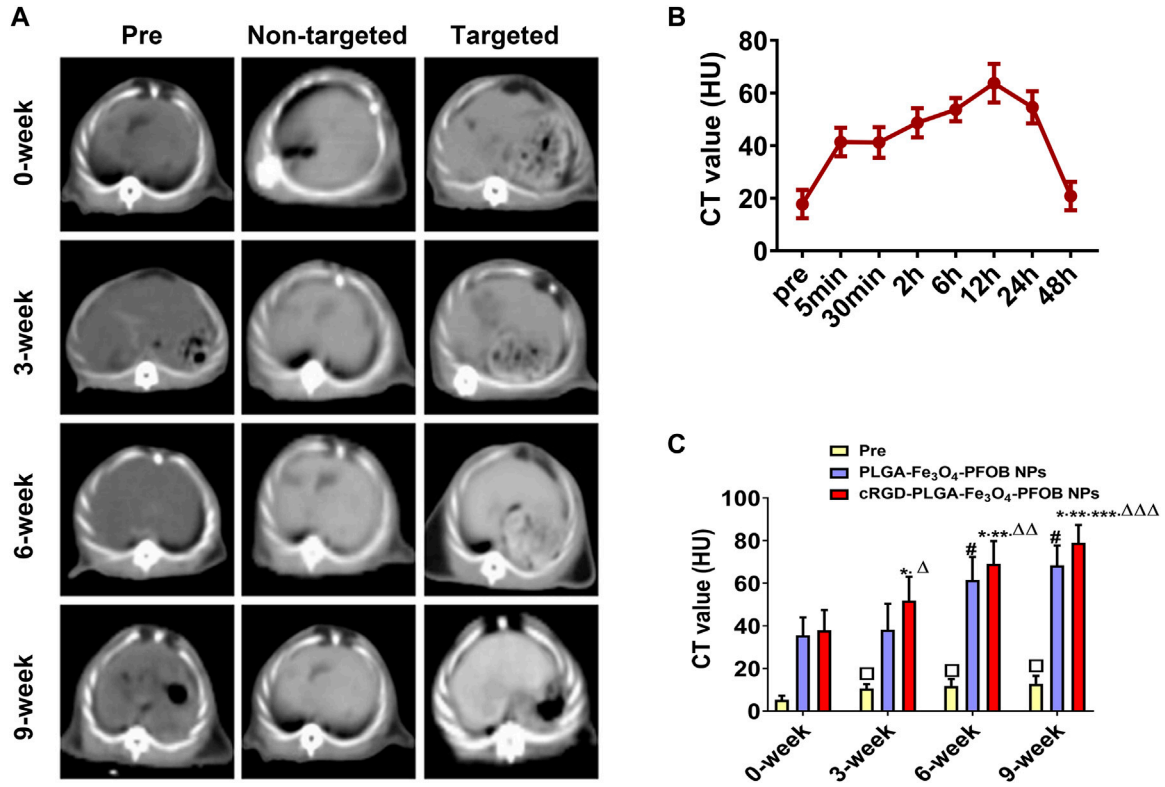

FIGURE 9
In vivo CT imaging. **(A)** CT images of liver before and after injection of targeted contrast agents (cRGD-PLGA-Fe_3O_4-PFOB NPs) or non-targeted contrast agents (PLGA-Fe_3O_4-PFOB NPs). **(B)** CT value of the liver parenchyma in the 0-week group within 48 h after injection of cRGD-PLGA-Fe_3O_4-PFOB NPs. **(C)** Comparison of liver CT values before and after injection of cRGD-PLGA-Fe_3O_4-PFOB NPs or PLGA-Fe_3O_4-PFOB NPs in each group (*p < 0.05 versus 0-week group, **p < 0.05 versus 3-week group, ***p < 0.05 versus 6-week group, #p < 0.05 versus 0-week or 3-week group, ΔP <0.05 versus non-targeted 3-week group, ΔΔP <0.05 versus non-targeted 6-week group, ΔΔΔP <0.05 versus non-targeted 9-week group, □p < 0.05 versus 0-week group).

different fibrotic groups and the normal control group prior to NP injection. The CT values of the fibrosis groups were no statistical difference but higher than those of the normal group. Moreover, T2 values in the 6-week and 9-week groups were significantly higher than those in the 3-week group and 0-week group. Prior literature reporting T2 values measurements of human fibrotic liver samples corroborate our results, showing a stepwise increase in T2 values with the progression of fibrosis (Guimaraes, et al., 2016). A possible explanation presented by literatures is that an increased inflammatory component in chronic liver disease is related to the etiology of this finding (Oo, et al., 2010; Anstee, et al., 2010).

Early measurements after injection may be inaccurate because they reflect the concentration of NPs in the blood pool rather than those in the ECM. We thus first observed the changes in the quantitative index of liver parenchyma in normal rats at different time points after intravenous injection. The T2 values reached the peak level 6 h post-injection, indicating that the NPs reached the maximum accumulation level in the ECM. Although the CT values and EI values at this time were not the highest point, they were still maintained at a high level (Figures 8B, 9B, 10B). Therefore, to ensure that the enhanced effect of NPs could be maintained at a high level with sufficient targeting time, the observation and comparison time point at which subsequent imaging experiments should be performed, were determined to be 6 h post-injection. Similar to the results of previous studies (Zhang, et al., 2016; Xuan, et al., 2017; Wu, et al., 2019; Wang, et al., 2011), quantitative index comparisons showed the EI and CT values increased, while the T2 values decreased as fibrosis progressed following cRGD-PLGA-Fe_3O_4-PFOB NPs injection (Figures 8C, 9C, 10C), which was indicative of greater accumulation of NPs due to the increased integrin $\alpha_v\beta_3$ expression in liver. These imaging results suggested that cRGD-PLGA-Fe_3O_4-PFOB NPs could act as novel tools to provide useful information for the identification of early liver fibrosis and noninvasive evaluation of liver fibrosis. An important advantage of this probe is that it combines independent biophysical properties measured by three imaging

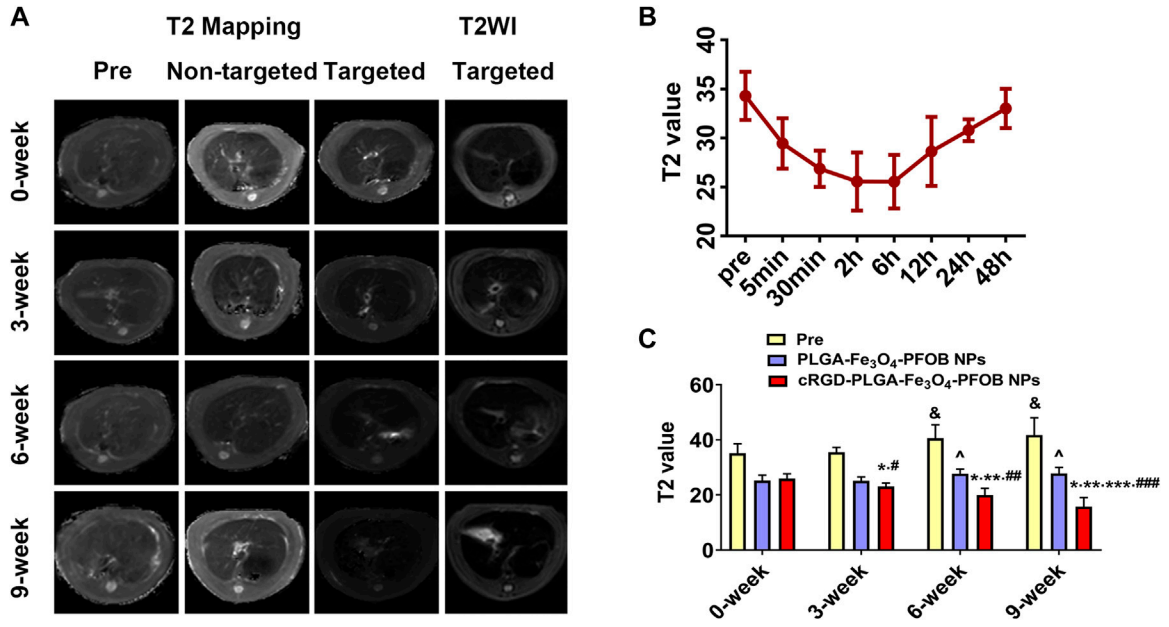

FIGURE 10
In vivo MR imaging. **(A)** MR images of liver before and after injection of targeted contrast agents (cRGD-PLGA-Fe_3O_4-PFOB NPs) or non-targeted contrast agents (PLGA-Fe_3O_4-PFOB NPs). **(B)** T2 value of the liver parenchyma in the 0-week group within 48 h after injection of cRGD-PLGA-Fe_3O_4-PFOB NPs. **(C)** Comparison of liver T2 values before and after injection of cRGD-PLGA-Fe_3O_4-PFOB NPs or PLGA-Fe_3O_4-PFOB NPs in each group (&$p < 0.05$ versus 0-week or 3-week group, ^$p < 0.05$ versus 0-week or 3-week group; *$p < 0.05$ versus 0-week group; **$p < 0.05$ versus 3-week group; ***$p < 0.05$ versus 6-week group; #$p < 0.05$ versus non-targeted 3-week group; ##$p < 0.05$ versus non-targeted 6-week group; ###$p < 0.05$ versus non-targeted 9-week group).

techniques, which offset the limitations of each measurement and generate broader and more feasible clinical application prospects.

Notably, both cRGD-PLGA-Fe_3O_4-PFOB NPs and PLGA-Fe_3O_4-PFOB NPs could be taken up by Kupffer cells, whereas cRGD-PLGA-Fe_3O_4-PFOB NPs could also be specifically taken up by aHSCs in fibrotic livers (Wang, et al., 2011). To prevent possible accumulation of NPs in the Kupffer cells from affecting the measured results, we designed a control group of rats with an equivalent degree of fibrosis that was received equal doses of PLGA-Fe_3O_4-PFOB NPs. Except for the normal group, the higher EI and CT values and lower T2 values were observed in rats injected with cRGD-PLGA-Fe_3O_4-PFOB NPs compared to rats injected with PLGA-Fe_3O_4-PFOB NPs, which was indicative of increased imaging effect due to the cRGD-medicated specific uptake by aHSCs. After the injection of PLGA-Fe_3O_4-PFOB NPs, significant differences in EI and CT values between the 9-, 6-week group and the 0-, 3-week groups were observed. Then, the EI values of 9-week groups were higher than those of the 6-week groups. The increased accumulation of NPs can be attributed to the following factors: First, macrophages that increased with liver fibrosis progression may phagocytose more NPs (Wattacheril, et al., 2018). Second, angiogenesis and revascularization increased parallel with the severity of fibrosis (Xu, et al., 2010; Niu, et al., 2013). These newly formed LSECs are defective because of the wide fenestrations and the absence of smooth muscle layers. Third, the abnormal architecture often lacks effective lymphatic drainage. Although these three theories suggest lower T2 values in advanced fibrotic liver after the injection of PLGA-Fe_3O_4-PFOB NPs, the T2 values of the 6- and 9-week groups were still higher than those of the 0-week and 3-week groups. We speculated that this phenomenon may be related to the smaller doses of NPs used in MR imaging than US and CT imaging and the limited encapsulation volume of Fe_3O_4 in PLGA, which resulted in an insufficient negative effect to offset the high T2 values in the 6- and 9-week groups prior to administration.

4 Conclusion

We showed expression levels of integrin $\alpha_v\beta_3$ increased with fibrosis severity in CCl_4 rat models, and the up-regulation level was more closely related to the activation of HSCs than neovascularization. In addition, our data demonstrated for the first time that combined US/CT/MR molecular imaging specifically target integrin $\alpha_v\beta_3$ by using cRGD-PLGA-Fe_3O_4-PFOB NPs was feasible for monitoring HSC activity and assessing liver fibrosis progression. The three techniques obtain complementary and different information with the potential to improve the diagnostic accuracy of a single imaging technique.

Data availability statement

The datasets presented in this study can be found in online repositories. The names of the repository/repositories and accession number(s) can be found in the article/Supplementary Material.

Ethics statement

The animal study was reviewed and approved by The Ethical Committee of Southwest Medical University.

Author contributions

JX and MA designed and funded the study, XT and XL conducted all the experiments and prepared the figures, ML, XZ, WF participated in the discussion. All authors approved the final version.

Funding

This work was financially supported by the Luzhou Municipal Science & Technology and Talent Bureau funds for applied and basic research of the People's Republic of China (2018-JYJ-44) and PhD research Start-up funds of the Affiliated Hospital of Southwest Medical University of the People's Republic of China (201,815), the National Natural Science Foundation of China (82,100,632), and Kuanren Talents Program of the Second Affiliated Hospital of Chongqing Medical University.

Conflict of interest

The authors declare that the research was conducted in the absence of any commercial or financial relationships that could be construed as a potential conflict of interest.

Publisher's note

Supplementary material

The Supplementary Material for this article can be found online at: https://www.frontiersin.org/articles/10.3389/fchem.2022.996116/full#supplementary-material

References

Andre, M., Nelson, T., and Mattrey, R. (1990). Physical and acoustical properties of perfluorooctylbromide, an ultrasound contrast agent. *Invest. Radiol.* 25, 983–987. doi:10.1097/00004424-199009000-00004

Anstee, Q. M., Concas, D., Kudo, H., Levene, A., Pollard, J., Charlton, P., et al. (2010). Impact of pan-caspase inhibition in animal models of established steatosis and non-alcoholic steatohepatitis. *J. Hepatology* 53, 542–550. doi:10.1016/j.jhep.2010.03.016

Cassinotto, C., Boursier, J., de Lédinghen, V., Lebigot, J., Lapuyade, B., Cales, P., et al. (2016). Liver stiffness in nonalcoholic fatty liver disease: A comparison of supersonic shear imaging, FibroScan, and arfi with liver biopsy. *Hepatology* 63, 1817–1827. doi:10.1002/hep.28394

Connolly, M. K., Bedrosian, A. S., Malhotra, A., Henning, J. R., Ibrahim, J., Vera, V., et al. (2010). In hepatic fibrosis, liver sinusoidal endothelial cells acquire enhanced immunogenicity. *J. I.* 185, 2200–2208. doi:10.4049/jimmunol.1000332

Dong, Q., Yang, H., Wan, C., Zheng, D., Zhou, Z., Xie, S., et al. (2019). Her2-Functionalized gold-nanoshelled magnetic hybrid nanoparticles: A theranostic agent for dual-modal imaging and photothermal therapy of breast cancer. *Nanoscale Res. Lett.* 14, 235. doi:10.1186/s11671-019-3053-4

Friedman, S. L. (2008). Mechanisms of hepatic fibrogenesis. *Gastroenterology* 134, 1655–1669. doi:10.1053/j.gastro.2008.03.003

Guimaraes, A. R., Siqueira, L., Uppal, R., Alford, J., Fuchs, B. C., Yamada, S., et al. (2016). T2 relaxation time is related to liver fibrosis severity. *Quant. Imaging Med. Surg.* 6, 103–114. doi:10.21037/qims.2016.03.02

Horiguchi, N., Wang, L., Mukhopadhyay, P., Park, O., Jeong, W. I., Lafdil, F., et al. (2008). Cell type-dependent pro- and anti-inflammatory role of signal transducer and activator of transcription 3 in alcoholic liver injury. *Gastroenterology* 134, 1148–1158. doi:10.1053/j.gastro.2008.01.016

Jeong, W. I., Park, O., Radaeva, S., and Gao, B. (2006). STAT1 inhibits liver fibrosis in mice by inhibiting stellate cell proliferation and stimulating NK cell cytotoxicity. *Hepatology* 44, 1441–1451. doi:10.1002/hep.21419

Li, D., He, L., Guo, H., Chen, H., and Shan, H. (2015). Targeting activated hepatic stellate cells (aHSCs) for liver fibrosis imaging. *EJNMMI Res.* 571, 71. doi:10.1186/s13550-015-0151-x

Li, F., Song, Z., Li, Q., Wu, J., Wang, J., Xie, C., et al. (2011). Molecular imaging of hepatic stellate cell activity by visualization of hepatic integrin αvβ3 expression with SPECT in rat. *Hepatology* 54, 1020–1030. doi:10.1002/hep.24467

Li, F., Yan, H., Wang, J., Li, C., Wu, J., Wu, S., et al. (2016). Non-invasively differentiating extent of liver fibrosis by visualizing hepatic integrin αvβ3 expression with an MRI modality in mice. *Biomaterials* 102, 162–174. doi:10.1016/j.biomaterials.2016.06.026

Lin, Y. S. (2017). Ultrasound evaluation of liver fibrosis. *J. Med. Ultrasound* 25, 127–129. doi:10.1016/j.jmu.2017.04.001

Niu, C., Wang, Z., Lu, G., Krupka, T. M., Sun, Y., You, Y., et al. (2013). Doxorubicin loaded superparamagnetic PLGA-iron oxide multifunctional microbubbles for dual-mode US/MR imaging and therapy of metastasis in lymph nodes. *Biomaterials* 34, 2307–2317. doi:10.1016/j.biomaterials.2012.12.003

Okada, M., Katsube, T., Kumano, S., Kagawa, Y., Araki, T., Tsuda, N., et al. (2011). Unenhanced fat fraction ratios obtained by MR and enhanced T2* values with liver-specific MR contrast agents for diagnosis of non-alcoholic steatohepatitis in rats. *Acta Radiol.* 52, 658–664. doi:10.1258/ar.2011.100360

Oo, Y. H., Shetty, S., and Adams, D. H. (2010). The role of chemokines in the recruitment of lymphocytes to the liver. *Dig. Dis.* 28, 31–44. doi:10.1159/000282062

Patel, K., and Rockey, D. C. (2006). Clinical utility of biomarkers of liver fibrosis. *Gastroenterol. Hepatol.* 2, 48–57.

Petros, R. A., and DeSimone, J. M. (2010). Strategies in the design of nanoparticles for therapeutic applications. *Nat. Rev. Drug Discov.* 9, 615–627. doi:10.1038/nrd2591

Mattrey, R. F., Long, D. M., Multer, F., and Higgins, C. B. (1982). Perfluoroctylbromide: a reticuloendothelial-specific and tumor-imaging agent for computed tomography. *Radiology* 145, 755–758. doi:10.1148/radiology.145.3.7146408

Sanna, V., Siddiqui, I. A., Sechi, M., and Mukhtar, H. (2013). Resveratrol-loaded nanoparticles based on poly(epsilon-caprolactone) and poly(d, l-lactic-*co*-glycolic acid)–Poly(ethylene glycol) blend for prostate cancer treatment. *Mol. Pharm.* 10, 3871–3881. doi:10.1021/mp400342f

Shin, H. J., Yoon, H., Kim, M. J., Han, S. J., Koh, H., Kim, S., et al. (2018). Liver intravoxel incoherent motion diffusion-weighted imaging for the assessment of hepatic steatosis and fibrosis in children. *World J. Gastroenterol.* 24, 3013–3020. doi:10.3748/wjg.v24.i27.3013

Sun, R., Park, O., Horiguchi, N., Kulkarni, S., Jeong, W. I., Sun, H. Y., et al. (2006). STAT1 contributes to dsRNA inhibition of liver regeneration after partial hepatectomy in mice. *Hepatology* 44, 955–966. doi:10.1002/hep.21344

Tapper, E. B., and Loomba, R. (2018). Noninvasive imaging biomarker assessment of liver fibrosis by elastography in NAFLD. *Nat. Rev. Gastroenterol. Hepatol.* 15, 274–282. doi:10.1038/nrgastro.2018.10

Taymouri, S., and Taheri, A. (2016). Use of nanotechnology in diagnosis and treatment of hepatic fibrosis: A review. *Curr. Drug Deliv.* 13, 662–672. doi:10.2174/1567201812666150907115404

Tran, T. D., Caruthers, S. D., Hughes, M., Marsh, J. N., Cyrus, T., Winter, P. M., et al. (2007). Clinical applications of perfluorocarbon nanoparticles for molecular imaging and targeted therapeutics. *Int. J. Nanomedicine* 2, 515–526.

Turaga, R. C., Satyanarayana, G., Sharma, M., Yang, J. J., Wang, S., Liu, C., et al. (2021). Targeting integrin $\alpha_v\beta_3$ by a rationally designed protein for chronic liver disease treatment. *Commun. Biol.* 4, 1087. doi:10.1038/s42003-021-02611-2

Wang, F. S., Fan, J. G., Zhang, Z., Gao, B., and Wang, H. Y. (2014). The global burden of liver disease: The major impact of China. *Hepatology* 60, 2099–2108. doi:10.1002/hep.27406

Wang, Q. B., Han, Y., Jiang, T. T., Chai, W. M., Chen, K. M., Liu, B. Y., et al. (2011). MR imaging of activated hepatic stellatecells in liver injured by CCl_4 of rats with integrin targeted ultrasmall superparamagnetic iron oxide. *Eur. Radiol.* 21, 1016–1025. doi:10.1007/s00330-010-1988-z

Wattacheril, J., Issa, D., and Sanyal, A. (2018). Nonalcoholic steatohepatitis (NASH) and hepatic fibrosis: Emerging therapies. *Annu. Rev. Pharmacol. Toxicol.* 58, 649–662. doi:10.1146/annurev-pharmtox-010617-052545

Williams, R. (2006). Global challenges in liver disease. *Hepatology* 44, 521–526. doi:10.1002/hep.21347

Wu, Y., Li, Z., Xiu, A. Y., Meng, D. X., Wang, S. N., and Zhang, C. Q. (2019). Carvedilol attenuates carbon tetrachloride-induced liver fibrosis and hepatic sinusoidal capillarization in mice. *Drug Des. devel. Ther.* 13, 2667–2676. doi:10.2147/DDDT.S210797

Xu, J. S., Huan, J., Qin, R., Hinkle, G. H., Povoski, S. P., Martin, E. W., et al. (2010). Synthesizing and binding dual-mode poly (Lactic-co-Glycolic acid) (PLGA) nanobubbles for cancer targeting and imaging. *Biomaterials* 31, 1716–1722. doi:10.1016/j.biomaterials.2009.11.052

Xuan, J., Chen, Y., Zhu, L., Guo, Y., Deng, L., Zheng, Y., et al. (2017). Ultrasound molecular imaging with cRGD-PLGA-PFOB nanoparticles for liver fibrosis staging in a rat model. *Oncotarget* 8, 108676–108691. doi:10.18632/oncotarget.21358

Yoon, Y. J., Friedman, S. L., and Lee, Y. A. (2016). Antifibrotic therapies: Where are we now? *Semin. Liver Dis.* 36, 087–098. doi:10.1055/s-0036-1571295

Zhang, C., Liu, H., Cui, Y., Li, X., Zhang, Z., Zhang, Y., et al. (2016). Molecular magnetic resonance imaging of activated hepatic stellate cells with ultrasmall superparamagnetic iron oxide targeting integrin $\alpha_v\beta_3$ for staging liver fibrosis in rat model. *Int. J. Nanomedicine* 11, 1097–1108. doi:10.2147/IJN.S101366

Zhang, X., Guo, Q. Y., Shi, Y., Xu, W., Yu, S., Yang, Z., et al. (2017). 99mTc-3PRGD2 scintigraphy to stage liver fibrosis and evaluate reversal after fibrotic stimulus withdrawn. *Nucl. Med. Biol.* 49, 44–49. doi:10.1016/j.nucmedbio.2017.02.004

Zhou, X., Murphy, F. R., Gehdu, N., Zhang, J., Iredale, J. P., and Benyon, R. C. (2004). Engagement of αvβ3 integrin regulates proliferation and apoptosis of hepatic stellate cells. *J. Biol. Chem.* 279, 23996–24006. doi:10.1074/jbc.M311668200